Energetic condensation growth of Nb thin films

M. Krishnan, E. Valderrama, and C. James
Alameda Applied Sciences Corporation (AASC), San Leandro, California 94577, USA

X. Zhao, J. Spradlin, A-M Valente Feliciano, L. Phillips, and C. E. Reece
Thomas Jefferson National Accelerator Facility (Jefferson Lab), Newport News, Virginia 23606, USA

K. Seo
Norfolk State University (NSU), Norfolk, Virginia 23504, USA

Z. H. Sung
Applied Superconductivity Center, Florida State University (FSU), Tallahassee, Florida 32310, USA
(Received 6 December 2011; published 23 March 2012)

This paper describes energetic condensation growth of Nb films using a cathodic arc plasma, whose 60–120 eV ions penetrate a few monolayers into the substrate and enable sufficient surface mobility to ensure that the lowest energy state (crystalline structure with minimal defects) is accessible to the film. Heteroepitaxial films of Nb were grown on *a*-plane sapphire and MgO crystals with good superconducting properties and crystal size (10 mm × 20 mm) limited only by substrate size. The substrates were heated to temperatures of up to 700°C and coated at 125°C, 300°C, 500°C, and 700°C. Film thickness was varied from ~0.25 μm to >3 μm. Residual resistivity ratio ($\langle$RRR$\rangle$) values (up to a record $\langle$RRR$\rangle$ = 587 on MgO and $\langle$RRR$\rangle$ = 328 on *a*-sapphire) depend strongly on substrate annealing and deposition temperatures. X-ray diffraction spectra and pole figures reveal that RRR increases as the crystal structure of the Nb film becomes more ordered, consistent with fewer defects and, hence, longer electron mean-free path. A transition from Nb(110) to Nb(100) orientation on the MgO(100) lattice occurs at higher temperatures. This transition is discussed in light of substrate heating and energetic condensation physics. Electron backscattered diffraction and scanning electron microscope images complement the XRD data.

DOI: 10.1103/PhysRevSTAB.15.032001 PACS numbers: 74.78.−w, 52.80.Mg, 68.55.−a, 81.15.Aa

I. INTRODUCTION

This paper is organized as follows: We begin with a brief description of ''energetic condensation'', followed by a description of our cathodic arc deposition apparatus. Next we present $\langle$RRR$\rangle$ and T_c measurements in Nb thin films that were grown on *a*-sapphire and MgO crystal substrates. The $\langle$RRR$\rangle$ is here defined [1] as the ratio of resistivity at 300 K to that at 10 K, averaged across the film thickness. This bulk averaged $\langle$RRR$\rangle$ is different from the local RRR (at any depth in the film) because our measurement averages the RRR across the film. The $\langle$RRR$\rangle$ measurements are compared with a conceptual model that shows that the RRR at the surface of the films is higher than that measured through the bulk. We have measured RRR values in Nb thin films produced by energetic condensation techniques that match bulk Nb values (>300) for the first time. Next we show XRD data (Bragg-Brentano spectra and pole figures) from the Nb films and describe how the crystallographic orientation and quality are affected by deposition conditions. This is followed by presentation of electron backscattered diffraction (EBSD) data for the films. These data include both surface and cross-section EBSD images that are discussed in light of deposition conditions. TEM and atomic force microscope (AFM) images shed light on the surface roughness of the films and demonstrate good adhesion as well as high film density right from the first few monolayers of growth. Of particular interest are cross-section scanning electron microscope (SEM) images of Nb films taken through so-called macroparticles of Nb that are part of the film growth. Cathodic arc plasmas are known [2] to produce both energetic ions (60–120 eV with 3+ charge in the case of Nb) as well as ~0.1–10 μm macroparticles. These macroparticles are at or near the melt temperature of Nb and therefore have much lower velocity/Nb atom than do the faster ions. Yet the crystal structure and density of the macroparticle regions of the Nb film are identical to those of the adjacent regions on the film that were grown by impingement of ~100 eV triply charged ions (energetic condensation). The remarkable similarity in the two film regions is discussed in light of an energetic ion-induced seed layer that governs subsequent crystal growth. Comparison with related work published by Kniesel

Published by the American Physical Society under the terms of the Creative Commons Attribution 3.0 License. Further distribution of this work must maintain attribution to the author(s) and the published article's title, journal citation, and DOI.

et al. on bulk Nb cavities [3,4] suggests a new technique for Nb single crystal growth on the insides of superconducting radio frequency (SRF) cavities using a hybrid approach: first create a high quality single crystal seed layer of Nb(100) on bulk Nb using our energetic condensation process, followed by growth of a thicker film by condensing pure molten Nb on the seed layer. This work has also studied Nb crystal growth on *c*-sapphire and amorphous borosilicate substrates, the results of which have been published elsewhere [5]. The ability of our energetic condensation process to drive crystal growth on an amorphous substrate has implications for future development of cast Al SRF cavities that have high quality, superconducting Nb thin films on their inside surface. We conclude this paper with a discussion of the differences between our energetic condensation process and other processes, such as electron cyclotron resonance (ECR) plasma deposition [6] or much lower energy film growth processes such as magnetron sputtering and e-beam evaporative deposition.

II. ENERGETIC CONDENSATION

This paper describes energetic condensation growth of Nb films using a cathodic arc plasma. Such a plasma uses a low voltage (~30 V) arc discharge to generate a highly ionized plasma [7], the ions of which consist exclusively of the cathode material. The plasma is created in a vacuum arc discharge, so can be sustained in otherwise ultrahigh vacuum ($\sim 10^{-8}$ Torr) conditions. For Nb plasmas, the ion energy spectrum has been measured [8] to lie in the range of 60–120 eV, with most of the ions being triply charged. When such energetic ions impinge in the normal direction upon a substrate, they penetrate and deposit their energy within a few monolayers from the surface. The net energy deposited is in the range of 100–170 eV, as the $\approx$ 46 eV of ionization potential energy carried by Nb^{3+} is added to the kinetic energy. This energy range greatly exceeds typical binding energies in the lattice (~10 eV), so substrate atoms are displaced and the excess energy goes into electronic and phonon excitations. These ion deposition processes occur on a rapid time scale of <1 ps. This time scale may be estimated as follows: the range of Nb ions in sapphire or MgO substrates is ~1 nm (a few monolayers). The fastest incident ions with ~14 km/s speeds (100 eV energy) that are stopped after a single binary collision in the lattice would travel for ~1 nm/14 km/s = 70 fs. Slower ions moving at ~4 km/s (10 eV) and suffering many inelastic collisions before stopping might cover a distance of ~3 nm and thus take $\approx$ 0.75 ps. Lifshitz *et al.* [9] and Brice *et al.* [10] have described the details of the interaction between energetic ions (~100 eV) and various substrates. They have coined the term ''subplantation'' to distinguish this regime of ion-surface interactions from deep implantation (>1 keV ions) and surface interactions (<1 eV). In subplantation, the incident ions deposit more than enough energy into just a few subsurface atomic layers to displace atoms from the lattice and create interstitials. The key to effective subplantation is to maximize the number of displacements within this subsurface layer, while minimizing deeper defects. This is because the ion energy deposition (that occurs on ~1 ps time scales) must be accompanied by substrate heating. This heating allows subsurface defects (lattice dislocations, voids, and impurities) to migrate to the surface where they are annihilated. Such a synergistic interplay between the highly nonequilibrium ion deceleration physics in the top few atomic layers and thermal diffusion physics in the bulk, promotes growth of the film in a low energy state that is likely to be epitaxial growth, evolving as the film thickens, to homoepitaxial growth. Our pulsed discharge is fired once every few seconds, so the synergistic effects of fast ion deposition and thermal annealing are completed on each pulse.

Alameda Applied Sciences Corporation (AASC) and Jefferson Lab conduct research into SRF thin film coatings that are grown using energetic condensation (EC) a term used to represent three complementary approaches: a UHV cathodic arc process, an ECR source process, and high power impulse magnetron sputtering. These sources deliver ions to the coated surface that have ~100–200 eV energy. In the case of the cathodic arc, the Nb ions are triply charged and have kinetic energy spread over 60–120 eV. In the case of the ECR source, the typical singly charged Nb ion energy is ~60 eV. A bias of ~100–120 V increases the energy to ~160–180 eV at the substrate. In the case of either the vacuum arc or the ECR, the energy is easily varied by varying the substrate bias voltage. But there are subtle differences in the ion spectra. The coaxial energetic deposition (CED) spectrum is broad and ranges from ~20 eV up to ~170 eV, whereas the ECR spectrum would be a more narrow spectrum with only a ±10 eV spread about the mean. Then too, the angular spread of the incident ions is also important as the range of ions in the solid varies strongly with angle.

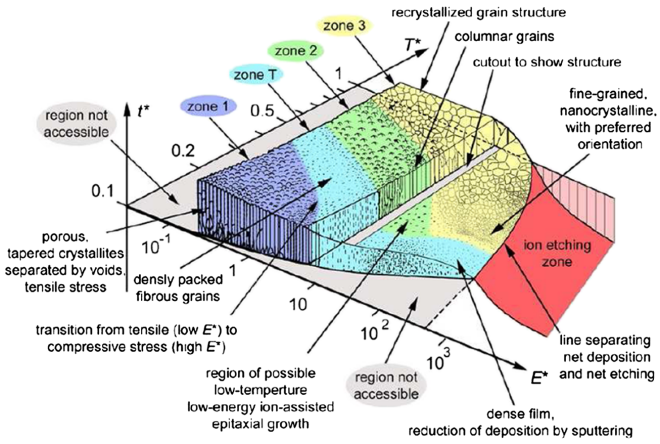

FIG. 1. SZD for ion-assisted vacuum deposition (reproduced from Ref. [12] with permission from Elsevier publishers).

Thornton [11] presented a structure zone diagram (SZD) to describe the interplay between thermal and kinetic energy driven film growth in thin films. This SZD is applicable to processes in which the source plasma is created in a partial pressure of noble gas such as argon. Anders [12] (see Fig. 1) has offered a variation on the SZD that is more appropriate for vacuum deposition. In this case, Thornton's pressure axis is replaced by an energy axis. Zone 2 of Fig. 1 (reproduced from Ref. [12]) shows that high energy ions effectively permit low-temperature ion-assisted epitaxial growth. This paper presents several examples of such epitaxial growth of Nb films on various substrates.

III. MOTIVATION FOR SUPERCONDUCTING THIN FILM DEVELOPMENT

Most rf particle accelerators worldwide utilize rf cavities made from a conventional conductor such as copper to accelerate the particle beam. A few large research accelerators such as the Continuous Electron Beam Accelerator Facility (CEBAF) at Thomas Jefferson National Accelerator Facility (Jefferson Lab, or JLab), the Spallation Neutron Source (SNS), the Large Hadron Collider (LHC), and the European X-FEL under construction in Hamburg all use SRF accelerating cavities. SRF cavities consume less power than conventional cavities to produce a given accelerating gradient, even when the additional energy cost of the cryogenics system is taken into account [13]. However, the cryogenics system costs do represent a significant portion of the operating expense of SRF accelerators. Operation at higher temperature would reduce those costs. Niobium, the only presently accepted superconductor for SRF accelerators, has a transition temperature T_c of 9.3 K, but a practical operating temperature of 2 K at the typically used 1.3–1.5 GHz rf frequencies. Operation well below T_c is required to minimize surface resistance and maximize critical magnetic field. Increasing the operating temperature of the accelerator from 2 to 4.5 K could cut the cryogenics system costs in half, but would, at these rf frequencies, require use of an alternative superconductor with a higher transition temperature. Since the rf (London) penetration depth into the cavity surface is only $\sim$50 nm, it is of interest to develop thin film coatings on the nanoscale ($\sim$100 nm) for particle accelerators. One approach to reducing SRF accelerator costs is to replace the expensive, bulk Nb ($\sim$\$300/lb) cavities with a Nb thin film deposited on a less expensive material, such as Cu ($\sim$\$3/lb) or better yet, Al ($\sim$\$1/lb). The added advantage of Al over Cu is that the cavity can be cast instead of being machined, further reducing cost. Thin film coatings have the potential to reduce costs for many major upcoming SRF accelerators such as the International Linear Collider (ILC) and the Facility for Rare Isotope Beams and a potential muon collider. Especially at the lower rf frequencies of 200–500 MHz, the cavity cells are so large that bulk Nb might be prohibitively expensive, so Nb coated Cu or Cu alloys might be the more cost-effective option for operation at 4.5 K [14].

Pioneering work [15,16] on Cu cavities coated with Nb thin film has been done at the European Organization for Nuclear Research, known as CERN. By 1998, 272 copper 352 MHz cavities, Nb thin film coated via magnetron sputtering, were deployed for the Large Electron-Positron Collider (LEP-II) project. The circular LEP-II collider, with a circumference of 27 kilometers, was one of the largest particle accelerators ever constructed and has recently been replaced by the Large Hadron Collider (LHC). Future accelerator facilities, such as the proposed ILC, require high accelerating field $\sim$35 MV/m and $Q \geq 10^{10}$. It was reported in follow-on work at CERN [17,18] that at 1.5 GHz and 1.7 K the Nb thin film cavities for LEP had Q-drop to below 10^{10} at $\approx$ 15 MV/m and to below 5×10^9 at $\approx$ 20 MV/m. There is a motivation to better understand these limits and to improve Nb thin films' performance for future SRF accelerator cavities.

Our energetic condensation results point to a better way to coat Cu cavities than by using magnetron sputtering. The bulk-Nb like RRR values measured in our thin films, as well as the good crystal structure, high density, and low impurity content allow us to progress from the coupon level depositions made to date towards a Cu cavity coating using our CED apparatus. This is our next milestone. The payoff of higher temperature SRF cavities and cavities made out of thin film coated Cu or Al has motivated a multiyear research program at Alameda Applied Sciences Corporation (AASC) and JLab. The goal is to utilize energetic condensation to produce Nb-on-Cu films of sufficient quality to determine if the thin film rf properties are adequate for high power SRF applications such as particle accelerators. Thorough characterization of the surface morphology and rf properties of Nb-on-Cu is a necessary first step toward qualifying Nb coated Cu SRF cavities. Given the high cost ($>$\$100 M) and infrequent occurrence of large SRF accelerator upgrades and construction, it is difficult to imagine acceptance of an alternative superconductor in SRF accelerators without demonstrated performance equivalent to (or better than) that of bulk Nb (2 K). Implementation of Nb-on-Cu coated cavities into commercial accelerators, our long-term goal, is likely to follow reliable operation in a research laboratory setting.

IV. EXPERIMENTAL CONFIGURATION

There are two experimental configurations at AASC. Figure 2 shows a photograph of the coaxial energetic condensation (CED^{TM}) apparatus [19] with a 2.2 GHz copper rf cavity adjacent to it, shown for scale.

Figure 3 is a schematic drawing of the operation of the CED^{TM} apparatus. The arc is formed between an on-axis cathode (1-cm diameter and 60 cm long) and a coaxial mesh anode (4-cm diameter and 45 cm in length). The arc

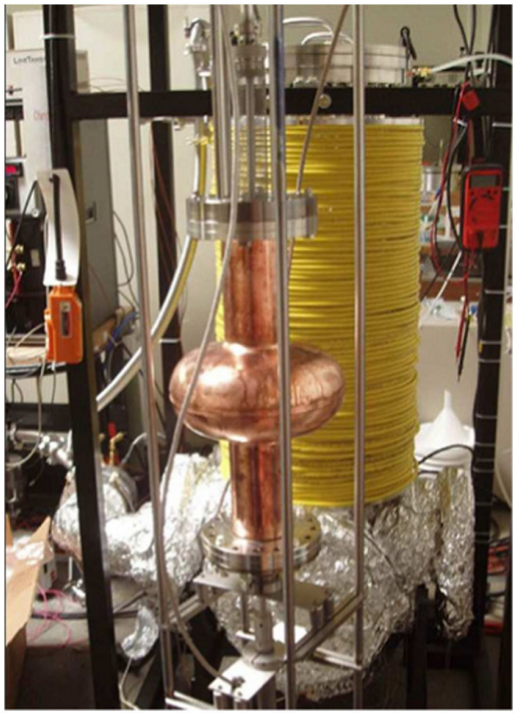

FIG. 2. Photograph of the CED™ system, showing a 2.2 GHz copper rf cavity for scale.

is sustained by a PowerTen, Inc. power supply (100 V, 200 A). The repetition rate of the arc is 0.5 Hz, limited at present by silicon controlled rectifier switches, but may be increased by using insulated gate bipolar transistor switches to more rapidly turn off the arc between pulses.

The arc is triggered by a proprietary trigger system. The substrate is placed outside the mesh anode. The entire assembly is enclosed in a 25-cm diameter ConFlat vacuum spool. The vacuum spool is double walled with a solenoid wound on the outside. The solenoid is capable of producing a peak magnetic field of 10 mT in either the z^+ or the z^- direction. The arc current is controlled by adjusting a ballast resistor in series with the cathode. This system is equipped with a substrate heater and temperature control

FIG. 4. Photograph of cathodic arc deposition (CAD) facility at AASC.

system that is capable of operation up to 1200°C. The key process variables are substrate temperature, degree of annealing, substrate bias, deposition rate, and base pressure. Base pressures of $\sim 5 \times 10^{-9}$ Torr are possible within this chamber and are measured and monitored using a SRS200 residual gas analyzer. In addition to substrate temperature control, the substrate can also be biased.

Figure 4 shows a photograph of the cathodic arc deposition (CAD) facility available at AASC.

Two pulse forming networks (PFNs) are shown in the figure. These PFNs allow independently triggered arcs to be driven in two separate cathodes, with a common mesh anode. Figure 5 shows a photograph of the dual-target arrangement. This arrangement allows growth of superconducting films of A-15 compounds such as Nb_3Sn, Mo_3Re [20] etc., as well as MgB_2 films.

The film deposition rate in the CAD source was measured by measuring the thickness profile of a deposited Nb film. A 75-mm diameter masked borosilicate glass witness plate was located 40-mm from the 10-mm diameter cathode. After 7000 pulses of 500 A/1 ms, the thickness profile shown in Fig. 6(a) was obtained using a DEKTAK profilometer.

Simple bookkeeping allows determination of the growth rate as shown in Fig. 6(b). The Nb plasma is formed from tiny cathode spots that typically carry ~100 A at most. Each spot lasts for ~1 μs and hence the spots dance all over the 10-mm diameter cathode during the 1 ms pulse.

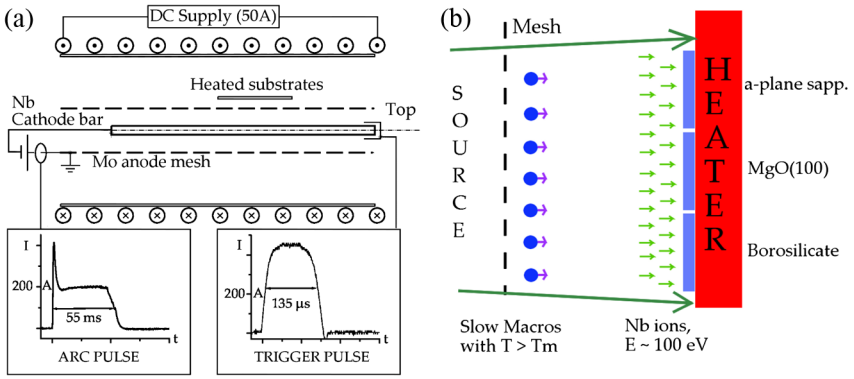

FIG. 3. Schematic drawing of CED™ operation: (a) coaxial electrode geometry and typical current pulses to trigger and arc; (b) detail of anode mesh and heated substrate, showing plasma transmitted by the anode onto the substrate.

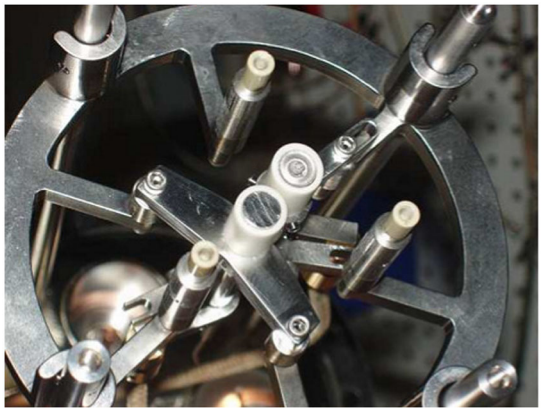

FIG. 5. Photograph of dual-cathode cathodic arc deposition (CAD) facility at AASC.

Viewed from afar, the plasma appears to emanate from a ~10-mm spot. The expansion into vacuum of such a plasma is supersonic and the plasma expands into a cone of half-angle $\approx 30°$. The red curve in Fig. 6(a) is a Gaussian fit to the thickness profile. The integral of the mass under this profile was calculated as 7.3 μg/pulse, as shown in the first row of the table in the figure. From the known charge/pulse and the transparency of the mesh anode, the erosion rate of Nb at the cathode was estimated to be 21 μg/C, a value that agrees with published literature [21]. The next row of the table shows the peak film thickness/pulse, as 0.56 nm. Note that this is ≈ 1 atomic layer/pulse. But the pulse lasts only 1 ms. Hence, the instantaneous deposition rate is 560 nm/s. To put this in perspective, the instantaneous flux of Nb ions (triply charged) to the substrate may be estimated from the mass

(a)

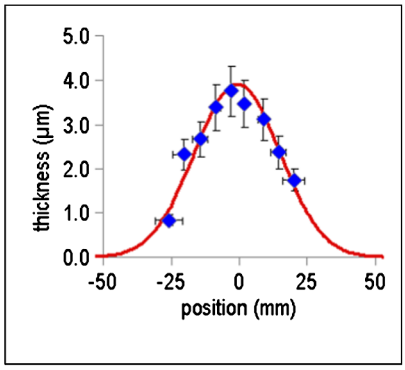

(b)

mass/shot=	7.3	μg
charge/shot=	0.5	C
anode transmission.=	0.7	
erosion rate=	21	μg/C
peak thickness/pulse=	0.56	nm
instant. rate=	560	nm/s
instant. flux of Nb ions=	1.03×10^{18}	Nb ions/cm²-s

FIG. 6. Measured Nb film thickness profile (a) and derived growth rate (b) for CAD coating apparatus.

deposited/pulse, the effective spot size over which this mass is deposited, and the pulse width. The estimated flux is 10^{18} Nb ions/cm^2-s. Such a high flux, combined with the high energy deposited into the first few monolayers of the substrate, is capable of significant modification of that surface. Nb ions will be deposited into the substrate as interstitials, displacing existing atoms and forcing a rearrangement of the lattice. Under the right conditions of substrate annealing and heat treatment, epitaxial growth of the Nb film is observed. But what happens to this heteroepitaxy when the Nb grows on a dissimilar substrate such as sapphire, MgO or Cu? At the rate of 0.56 nm/pulse, after just ten pulses, a layer of ≈ 5.6 nm will have grown. Subsequent pulses deliver Nb ions that deposit their energy into a subsurface layer that consists almost exclusively of Nb atoms. Our films are typically ~1–5 μm thick. Thus, although the initial stage of growth of the Nb film is denoted as heteroepitaxy, for thicker films, the growth transitions from heteroepitaxy to homoepitaxy after a certain film thickness. Energetic condensation drives this transition and enables pure crystals of Nb to be grown on rather dissimilar substrates, as shown below. The deposition rate is easily controlled since the mass liberated from the cathode is directly related to the total charge transferred by the arc. The charge transfer increases by increasing the magnitude and/or the duration of the current.

V. ⟨RRR⟩ AND T_c MEASUREMENTS

Nb thin film depositions were carried out in the CED™ apparatus on *a*-plane sapphire and MgO substrates. Several tools were used to characterize the films: SEM, XRD, EBSD, cross-section EBSD, TEM, and AFM. The details of the ⟨RRR⟩ measurement and results obtained in Nb films on MgO are published elsewhere [19]. Here we show companion results obtained on *a*-sapphire and repeat selected MgO data for completeness. A multiple-sample four-point-probe testing platform was used to measure the thin film material's transition temperature T_c and the residual resistivity ratio (⟨RRR⟩). The RRR is defined [11] as the ratio of resistivity at 300 K to that at 10 K. An ac or dc current runs through the sample via two poke pins (#1 and #4), and the small voltage signal dropped on two intermediate poke pins (#2 and #3) is measured using either a high-speed high-dynamic-range data acquisition system (National Instruments™), a commercial lock-in amplifier (Stanford Instruments™ SR530), or a commercial nanovoltmeter (Keithley™). The processes of sample multiplexing, data acquisition, and temperature recording are controlled using a customized LabView™ automation program. Since the pin 2–3 differential voltage is proportional to the material's resistivity, ⟨RRR⟩ is measured as the ratio of the differential voltage at 300 K to that at 10 K. The test fixture and up to 16 samples were inserted into a vacuum-sealed Dewar and cooled by liquid helium down

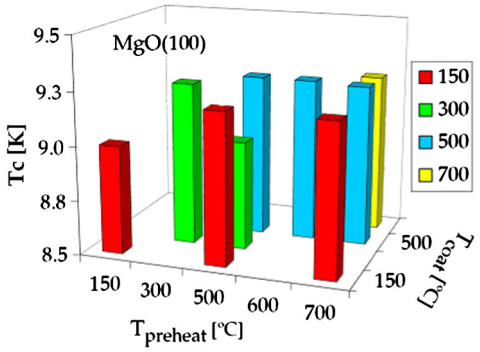

FIG. 7. T_c in ~1.5 μm Nb films grown on (100) MgO.

towards 4 K. By warming up the samples slowly, the pin 2–3 differential voltage was recorded as a function of temperature, which was measured by a Lakeshore Cernox™ sensor (resolution ~10 mK). The overall measurement error is 2%–10%. The crystal substrates were annealed for 3 h at temperatures of up to 700°C, while the temperature at which the (~1.5 μm thick) deposition was done was also varied from ≈ 150 up to 700°C. In what follows, for example, a substrate-anneal temperature $T_{\text{preheat}} = 300$°C followed by a coating at $T_{\text{coat}} = 150$°C is denoted by 300/150, etc.

Figure 7 shows a 3D plot of measured T_c in Nb films grown on MgO substrates. Figure 8 shows similar data for Nb films on *a*-sapphire substrates. The plots show a trend of increasing T_c (towards the ideal bulk value of 9.25 K) as the preheat and deposition temperatures are increased.

It is evident that annealing the substrates and heating them during deposition has a beneficial effect upon the T_c values. What was more remarkable was the strong effect that this heating had on ⟨RRR⟩, as presented next.

One example of a high ⟨RRR⟩ = 587 ± 1%, measured in a 5.5 μm thick film of Nb on MgO (100) is shown in Fig. 9.

Figure 10 shows a 3D plot of ⟨RRR⟩ for Nb films grown on *a*-sapphire. The RRR is denoted as ⟨RRR⟩ in what follows because our 4-point probe measurement is an

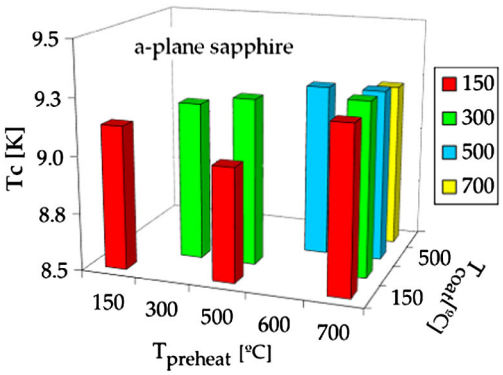

FIG. 8. T_c in ~1.5 μm Nb films grown on *a*-sapphire.

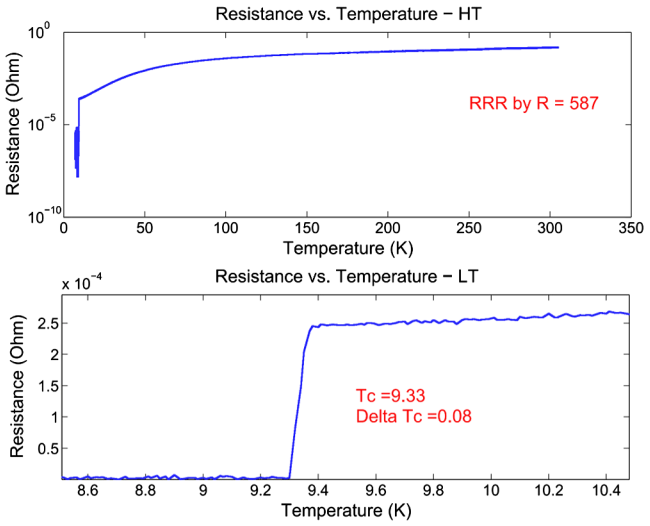

FIG. 9. ⟨RRR⟩ = 587 in 5.5 μm Nb film grown on (100) MgO.

average of the RRR across the ~few μm film thickness. In an earlier paper [19] we showed this average might be related to the local value nearer the surface of the film. It is evident that ⟨RRR⟩ increases rapidly (from 7 up to 333) as the substrate-annealing temperature and the deposition temperature are both increased. These data are for a fixed film thickness ~1 μm. Thicker samples showed still higher ⟨RRR⟩.

These measurements show that whereas 500/150 and 700/150 gave ⟨RRR⟩ < 10, 500/500 jumped to ⟨RRR⟩ = 40, while 600/500 gave ⟨RRR⟩ = 120. 700/500 gave the highest ⟨RRR⟩ value (150) but 700/700 dropped ⟨RRR⟩ down to 80. The data for Nb on MgO revealed a similar trend of very strong increase of ⟨RRR⟩ with preheat and coating temperatures as published elsewhere [19]. Both T_c and ⟨RRR⟩ show improvement with substrate heating.

In an earlier article [19] we presented a simple model for the variation of RRR with film thickness. The physical basis for this model is that as the film grows, the texture changes from fibrous, small-grained crystals to larger

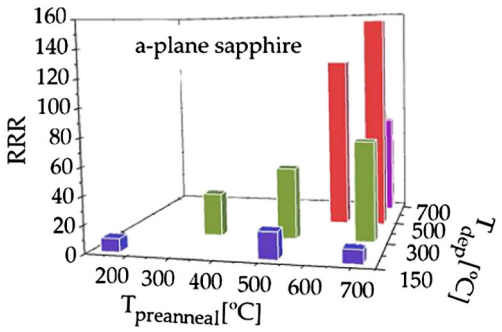

FIG. 10. ⟨RRR⟩ vs *a*-sapphire substrate-anneal temperature ($T_{\text{preanneal}}$ horizontal axis) and deposition temperature ($T_{\text{deposition}}$, depth axis). Note that all films were of the same thickness of ≈ 1 μm.

grains with higher crystalline order, due to the nonequilibrium subplantation effects of energetic condensation. With increasing grain size and fewer intergrain defects, the RRR should increase with thickness. But in the limit of a near-perfect single crystal, RRR must converge asymptotically to a limit that would correspond (in the superconducting state) to a finite residual resistivity. We had proposed an *ad hoc* expression for such a saturation of RRR in [SUST IOP]. There we estimated that the measured ⟨RRR⟩; of 585 in Nb on MgO might correspond to RRR = 680 at the surface.

To apply this model to the data on *a*-sapphire, we fix the RRR at 680 (the same value as was estimated for Nb-on-MgO) and vary the ''*e*-folding'' film thickness δ^* (the thickness at which the RRR has reached 68% of its peak saturated value). The results are shown in Fig. 11. The data are bounded by the range 2.9 μm$\langle\delta^*\rangle$2.5 μm. Similar fits to the Nb-on-MgO data gave 1.3 μm$\langle\delta^*\rangle$0.65 μm. These fits suggest that the Nb-on-MgO film reaches saturation more rapidly than does the Nb-on-a-sapphire film.

Andreone *et al.* [22] have provided insight into how RRR (although a normal state measurement) relates to superconducting properties. Of particular note is their discussion of the role of impurities and defects at grain boundaries on magnetic field penetration and on residual resistance. Attanasio [23] modeled superconducting polycrystalline thin films as a network of superconducting grains connected via Josephson junctions at the grain boundaries and derived useful relations for the residual resistance. His work was itself motivated by earlier work by Hylton and Vendiks [24,25]. These models showed that RRR should increase with thickness and were compared to measurements using diode and sputtered films to show the variation with grain size that was expected. Because the films analyzed by Attanasio were of low RRR, the suggested trend of increasing RRR with grain size does not show the saturation observed in our films on MgO [19] and the trend suggested for the *a*-sapphire films (Fig. 11). Our films grow into single crystals at higher temperatures, so our highest ⟨RRR⟩ measurements are made within a single grain, as opposed to the multigrain data analyzed by Attanasio.

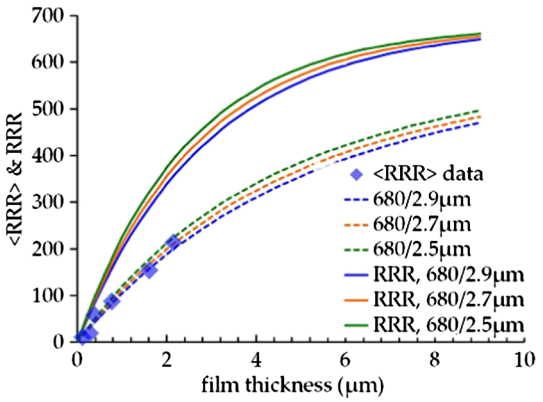

FIG. 11. Measured ⟨RRR⟩ (averaged over thickness) vs film thickness (blue diamonds); model fits to data: red dashed curve $\langle\text{RRR}\rangle = 400/\delta^* = 1.3$ μm; green dashed curve 390/1.1 μm; blue dashed curve 410/1.6 μm; upper solid curves are RRR (derived local value) vs thickness for the three cases noted in the legend.

Our *ad hoc* model for saturation is motivated by this earlier work. The higher ⟨RRR⟩ values in Nb-on-MgO vs Nb-on-sapphire are interesting. At first glance, just the opposite might have been expected, as the lattice mismatch between Nb(110) and the *a*-sapphire unit cell vs that of MgO is greatly in favor of the sapphire. Almost all prior literature describes Nb film growth on *a*-sapphire, since that material has very little lattice mismatch (1.7%) with Nb [110] and is available as highly polished substrates with good crystallinity. Historically, MgO has not been used for Nb film growth because its fcc structure has a 10.9% lattice mismatch for the bcc Nb [110] direction and 21.6% for the Nb [200] direction. We included MgO because its fcc structure was expected to better match to Cu. Our eventual goal is to first coat an MgO interface layer on Cu, followed by a Nb superconducting film. The insulator would serve not only as a crystal interface between Nb and Cu but would also inhibit vortex penetration [19]. Why are our results on MgO better than on *a*-sapphire? The incident ~100 eV ions of Nb^{3+} penetrate ~3 monolayers into the substrate and contribute their kinetic energy (plus the ~48 eV of ionization potential) to the creation of several lattice vacancies and phonon excitations, on a ~1 ps time scale. After the ~1 ms deposition pulse is over, the condensed Nb atoms rearrange themselves in a highly disturbed lattice that begins as a mix of substrate and incident atoms. The lowest energy states accessible to this volume are not necessarily driven predominantly by lattice mismatch, as occurs in low-temperature, surface epitaxial growth. This might be why the Nb-on-MgO film exhibits a smaller value of $\delta^* = 0.9$ μm vs the 2.7 μm for Nb-on-sapphire. The Nb-on-MgO film was observed [19] to change its orientation from Nb(110) to Nb(100) as the temperature of deposition was increased (> 500 C). The Nb(100) lattice is denser and excludes impurities better. MgO is also a getter which might further reduce impurity buildup in the film.

Until our recent work using energetic condensation, ⟨RRR⟩ values measured in Nb thin films grown using magnetron sputtering or e-beam evaporation were in the 10–80 range, with very few exceptions. Our demonstration of $\langle\text{RRR}\rangle = 587$ in Nb on MgO and 220 in Nb on *a*-sapphire, both potentially corresponding to a surface RRR of ~680, moves thin films into the realm of bulk Nb cavities. Next we present more data on the morphology of the films, to understand the dependence of ⟨RRR⟩ on substrate-anneal and deposition temperatures.

VI. XRD DATA FROM NB FILMS ON *a*- AND *c*-SAPPHIRE

Figure 12 shows XRD pole figures measured from Nb films that were grown on *a*-sapphire substrates. A typical deposition was preceded by annealing the substrate at 700°C for three hours, then growing the Nb film using the CED apparatus at various deposition temperatures. The principles of pole figure surveys can be found in an x-ray diffraction textbook [26]. For pole figure measurements, a point focus crossed-slit collimation was used. The secondary optics consisted of a 0.27° parallel-plate collimator followed by a flat graphite secondary monochromator and a proportional detector. A Soller slit was placed in front of the detector. Besides the conventional Bragg-Brentano survey (also known as the $\theta/2\theta$ survey), XRD pole figures in stereographic projection format were used to investigate ''texture'' (grain distribution in-plane) of every sample. A crystal plane in the ''real lattice space'' is a point in the ''reciprocal lattice space.'' The XRD pole figure technique uses a scattering vector to map such ''points'' in reciprocal lattice space. The difference between a diffracted and incident x-ray wave vector is defined as scattering vector. In pole figure coordinates, φ(0–360°) is the azimuth angle in-plane; ψ(0–90°) is the tilting angle between the scattering vector and the normal to the substrate surface. In such measurements, a scattering vector is programmed to gyrate in both coordinates to survey the positive hemispherical volume of a reciprocal lattice space. A film with random orientation would give a uniform distribution of scattering intensity. A single crystal film displays a spot pattern, and a film with restricted fiber texture displays a ring pattern of modulated intensity, tending toward a spot pattern with increasing degree of orientation.

Note that the diffuse peaks in the (110) pole figure for $\langle RRR\rangle = 10$ become much sharper (less texture) at $\langle RRR\rangle = 31$. The six lobes visible around the central pole in the figure are associated with twin symmetry in the epitaxial crystal, and are discussed elsewhere [27]. At the highest $\langle RRR\rangle = 155$, the sharpness of the lobes in the pole figure indicate that the Nb thin film is a single crystal with (110) crystal plane parallel to the substrate surface. The high crystallinity at the highest $\langle RRR\rangle$ might suggest fewer impurities and defects in the Nb lattice. These results demonstrate the ability to tailor the crystal structure and RRR (hence, defect and impurity concentrations) of Nb films by control of substrate thermal conditions, along with use of energetic condensation. Nb-on-MgO substrates showed a similar picture of better crystallinity with higher RRR and a remarkable transition from (110) to (100) orientation. Those results are published elsewhere [19].

Figure 13 shows pole figures for a Nb film grown on *c*-sapphire. As the RRR increases with substrate temperature from $\langle RRR\rangle = 16$ at 700/150 to $\langle RRR\rangle = 43$ at 700/700, the pole figures show a sharp transition from a rather diffuse (polycrystalline) structure to a sharp, single crystal Nb layer. The poles are so sharp at $\langle RRR\rangle = 43$ that arrows are used to guide the reader to their locations.

The XRD pole figures represent crystal structure averaged across the film thickness, because the Cu K-α x rays used penetrate the film and even the underlying substrate. By contrast, EBSD images show only surface grain and crystal structure and are discussed next.

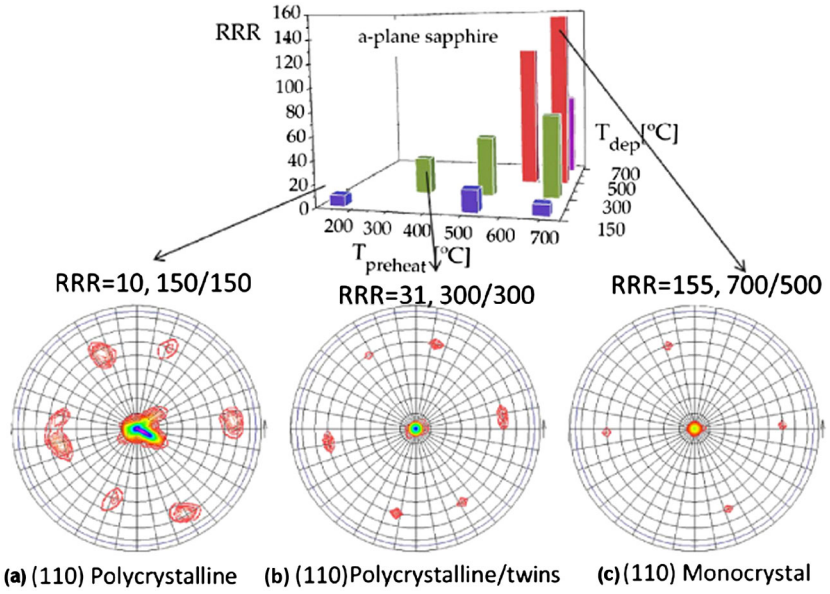

FIG. 12. XRD pole figures for Nb films grown on *a*-sapphire.

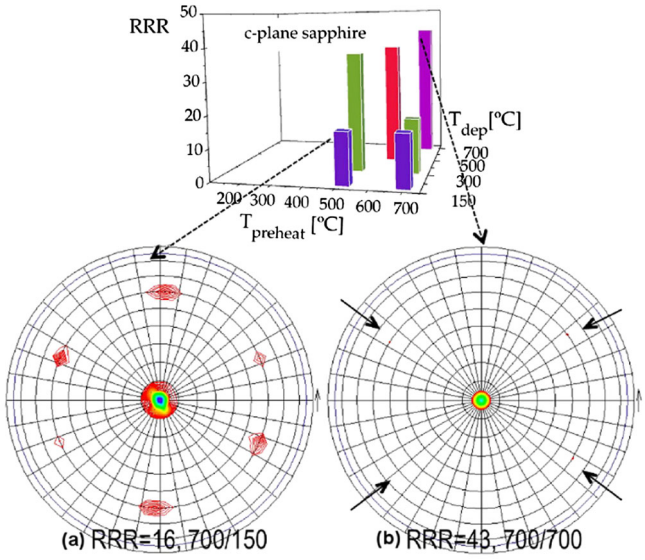

FIG. 13. XRD pole figures for Nb films grown on *c*-sapphire.

VII. EBSD IMAGES FROM Nb FILMS ON MgO AND ON *a*-SAPPHIRE

Figure 14 shows EBSD images superimposed upon SEM images of a Nb film grown on MgO, $\langle RRR \rangle = 196$ (500/500). The XRD pole figure is inset at bottom right.

The triangle at the top left shows the color code. The crystal structure consists of a mix of (110) and (100) orientations, shown at the 1 and 0.1 mm scales. The pole figure also shows this and suggests that the crystal structure is determined early in the film growth, but a cross-section EBSD image is needed to corroborate this assertion. Such cross-section EBSD images are shown in the next section.

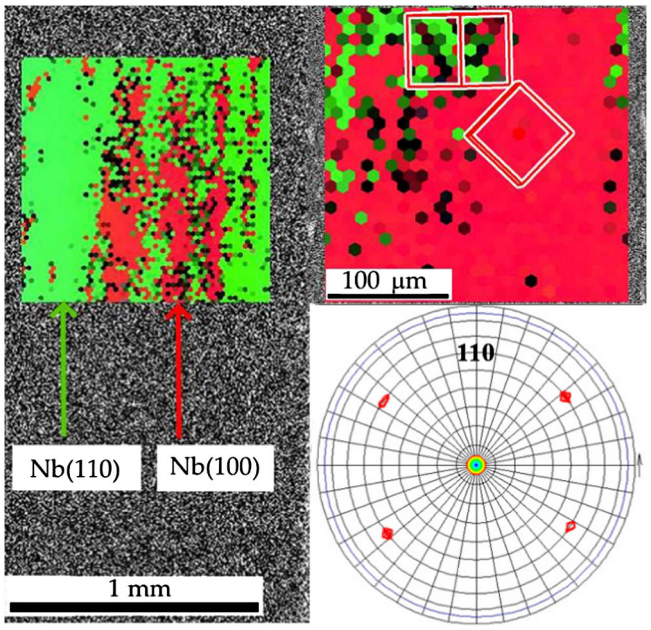

FIG. 14. EBSD images (superimposed upon SEM images) of Nb film on MgO(100) substrate. (XRD pole figure is at bottom right.)

But first we show EBSD images taken from a higher $\langle RRR \rangle = 333$ sample, in Fig. 15. The inset at bottom right shows a pole figure for a similar film but one that was coated at 700/700 and gave a $\langle RRR \rangle = 316$. At this higher RRR the Nb film has become a single crystal across the entire 10×10 mm substrate surface. The size of this crystal is limited only by the substrate size in this case. The EBSD (surface) image shows a pure (100) orientation. The pole figure in this case captures only the (200) plane, but that is in the same family as the (100) plane.

VIII. CROSS-SECTION EBSD IMAGES OF THIN FILMS

Figure 16 shows a cross-section EBSD image of a portion of a Nb film grown on MgO at 150/150 with $\langle RRR \rangle = 7$.

Starting from the MgO (001) substrate at the right, one observes at first a black region (indicating a confidence index $CI < 0.2$) followed by a mix of (001) and (101) planes (yellow and pink in the triangular color code inset in the figure). The black region could be amorphous Nb or simply a polycrystalline volume with grains too small to be resolved by the orientation imaging microscopy (OIM^{TM}) analysis system software that was used. The grains of Nb grow at an angle to the substrate and appear to get larger as the film is thicker. The low substrate temperature in this case does not allow epitaxial crystal growth, hence there is an amorphous or small-grained layer (~ 0.2 μm) that first grows on the MgO substrate. However, even for this low-temperature case, despite poor annealing of defects by heating, we see the effects of energetic condensation for thicker films. Beyond about 0.2 μm, the film gradually acquires larger grained crystal growth. Since the initial black layer is almost purely Nb, it is more appropriate to describe such growth as homoepitaxy. However, because the "seed" for nucleation and grain growth is a poor seed in this case, the subsequent crystal growth probably has a high defect density, poor intergrain boundaries and results in a low $\langle RRR \rangle = 7$. Figure 17 shows a dramatic difference at 500/500, when the $\langle RRR \rangle$ was increased to 196.

To keep the reader on her/his toes, we have reversed the SEM reference image in this case, so that the MgO is at left and the Nb film is to the right. In contrast to the image of Fig. 16, the Nb crystal growth begins immediately at the MgO surface. Cross-section EBSD images from four different locations on the film are presented, although only area A shows its associated SEM image. In each case, the Nb epitaxy is observed to be a mix of (001) and (101) (equivalent to 100 and 110 planes) beginning at the substrate surface. Area E shows that the grains grow larger with thickness. Area D shows an almost uniform 110 orientation. These cross-section images view the crystal orthogonal to the direction of view of the surface

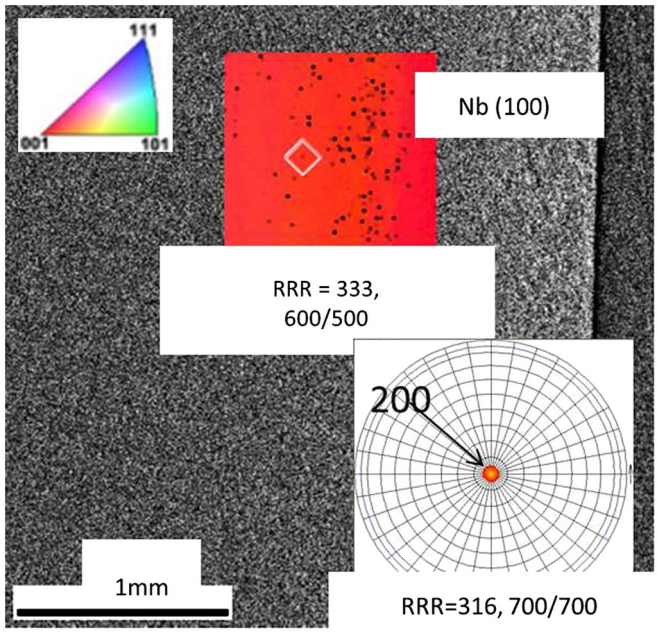

FIG. 15. EBSD image (superimposed upon SEM images) of Nb film (600/500) on MgO(100) substrate. XRD pole figure (700/700) is at bottom right.

EBSD, so the crystal planes plotted in the two cases will not correspond. The pink color seen from the surface [Nb(100)] appears green in the cross-section EBSD image. Correspondingly, the green Nb(110) seen from the surface is pink when viewed in cross section. These images corroborate the surface images presented in Fig. 14 and suggest that RRR increases with thickness because the grains become larger and defects are reduced. This is in accordance with the speculation of Andreone *et al.* [22] although they did not have the benefit of cross-section EBSD to corroborate their insightful assertions.

Figure 18 shows the cross-section images from Nb-on-MgO at 700/700, $\langle \mathrm{RRR} \rangle = 316$. These images indicate a uniform crystal orientation across the field of view. The smaller image to the right shows a finer scan using 150 nm steps, taken over a limited field of view indicated in the white square in the EBSD image to its left. The black zone indicates a poor CI that might be simply due to the grains being too small to be resolved. The 150 nm step-size scan shows that the highly crystalline Nb film grows around this impurity region and envelopes it. Beyond its surface, a pure crystal growth is observed. Again, we observe the synergistic effects of thermal annealing and energetic ion deposition in the film growth. What is not revealed at this scan step size is possible microscopic defects in the growing lattice that are gradually washed out as the film becomes thicker. That would potentially account for the strong dependence of RRR on film thickness. Note once more that the Nb(100) is green in this cross-section image, but would be represented as pink when viewed from the surface.

IX. COMPARISON OF Nb THIN FILMS WITH BULK Nb CAVITIES

Kneisel *et al.* [3,4] present Q-slope and quench data for several rf cavities fabricated out of small-grain, larger-grain, and single crystal Nb sheet metal. These authors describe a major difference in performance between single crystal/large grain cavities with primarily the (110) orientation at the surface vs (100). The (110) crystal cavity showed greater surface roughness after buffered chemical polishing (BCP) treatment and a Q-drop that did not disappear after even 12 hours of heat treatment. By contrast, the cavity with the (100) orientation had a smoother surface after BCP and gave the lowest Q-drop and highest quench fields of all cavities tested. Baars *et al.* [28] describe the different response to BCP chemicals of different Nb crystal orientations. Our results suggest the possibility of coating existing bulk Nb cavities with a thin film of Nb that is preferentially of the 100 orientation, thereby enhancing its high field performance. Our energetic condensation grows relatively thick films, ~few μm. The films are $\gg$ a few atomic layers thick, hence although the underlying substrate crystal structure might influence the

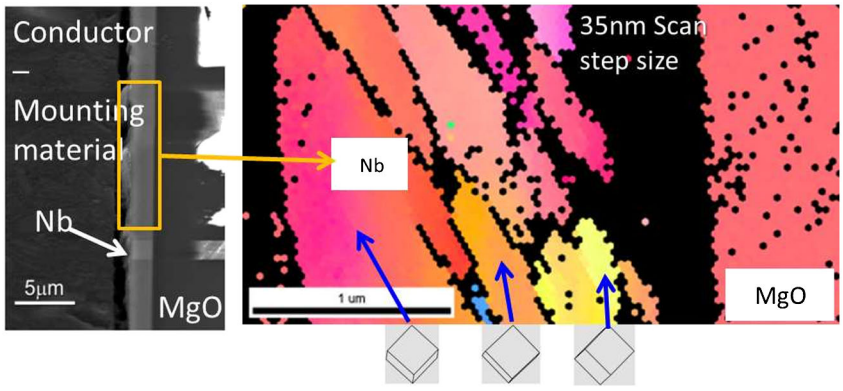

FIG. 16. Cross-section EBSD image of Nb film (150/150) on MgO, $\langle \mathrm{RRR} \rangle = 7$.

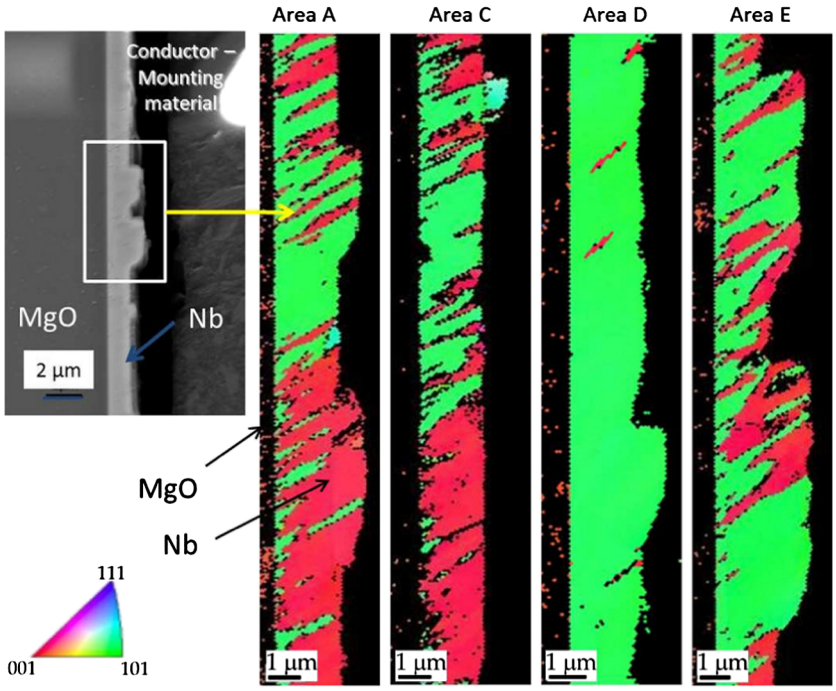

FIG. 17. Cross-section EBSD image of Nb film (500/500) on MgO, ⟨RRR⟩ = 196.

growth of the first few nm of film, energetic condensation, by disturbing the lattice, changes that lattice significantly and allows recondensation of Nb into lowest energy states that are accessible from the highly disturbed, nonequilibrium subsurface lattice. Beyond a certain film thickness (∼ few nm) subsequent growth is more akin to Nb growing on itself, rather than on the substrate lattice. From an epitaxial growth picture, we are essentially transitioning from heteroepitaxy at the start to homoepitaxy later, on crystalline substrates. On amorphous substrates, the

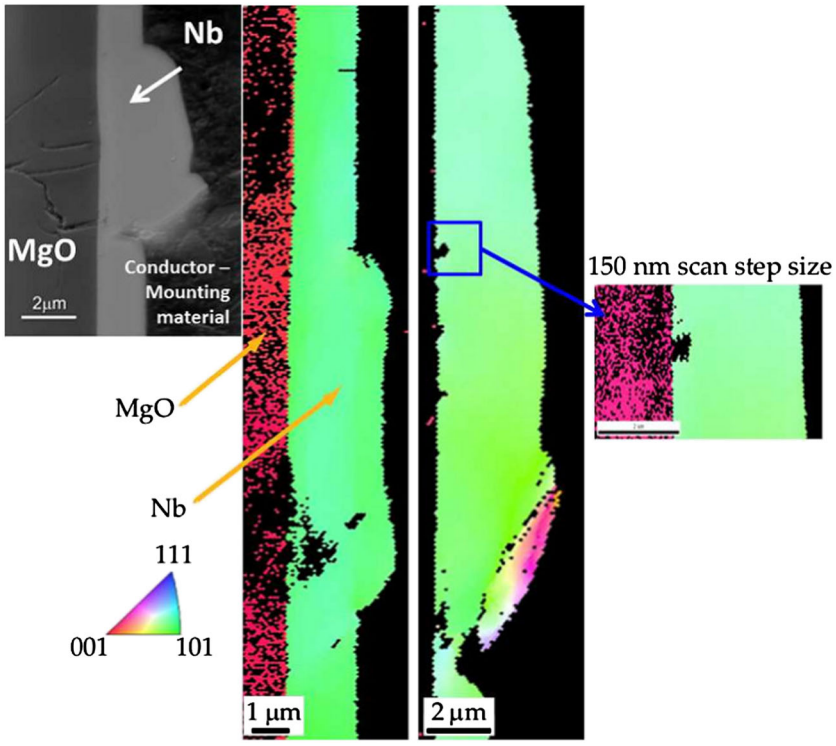

FIG. 18. Cross-section EBSD images of Nb film (700/700) on MgO(100) substrate.

energetic subplantation physics disturbs the amorphous subsurface and allows the condensing Nb atoms to organize themselves into a crystalline lattice [5]. We present here selected results to illustrate these arguments.

Two tests (dubbed CED-48 and CED-49) were conducted in which the first 500 pulses (120 nm of film growth) were at one substrate anneal/deposition condition, after which the test was resumed (after a ~5–10 hour interval) and a subsequent 1.5 μm film was deposited on the existing 120 nm film, but using very different anneal/deposition conditions. Halbritter [29] has pointed out that at pressures $>10^{-10}$ Torr and temperatures <1000 K, the Nb grows a 1–3 nm thick pentoxide layer. Hence, the new film grew on a Nb pentoxide layer that had inevitably grown on the initial 120 nm film during the few hour interval between tests. This pentoxide layer is amorphous and serrated and quite unlike the smooth crystalline MgO (100) substrate below it. We deliberately designed the two depositions to start with different "seeds," to wit: the first 120 nm of CED-48 film was grown at 150/150, corresponding to a highly textured Nb(110) lattice with poor RRR, but the first 120 nm of CED-49 was grown at 700/500, to promote a highly crystalline Nb(100) surface. However, after the few hours interval, the subsequent 1.5 μm film in CED-48 was grown at 700/500, whereas that for CED-49 was grown at 150/150. Cross-section EBSD images of these films would shed light on several features of film growth.

(i) How does the crystal structure evolve when starting with a serrated pentoxide surface rather than the MgO (100) crystal lattice? Does it follow the seed crystal layer below the pentoxide?

(ii) How is the RRR of the film affected by this growth?

The top portion of Fig. 19 shows EBSD images of the Nb films from these two tests. CED-48 shows Nb(110) whereas CED-49 shows Nb(100). To illustrate the effect of the seed layer on subsequent crystal growth, the bottom portion of the figure is a schematic representation of what the cross-section EBSD might show, had we taken such an image. CED-48 has a seed layer that was grown at 150/150 and is therefore polycrystalline, textured, and has the Nb(110) orientation. After the pentoxide layer had grown, subsequent growth occurred at 700/500, a condition normally conducive to single crystal Nb(100) growth. But the 1.5 μm film grows as Nb(110), mimicking the poor seed layer below the pentoxide. By contrast, the 1.5 μm new growth for CED-49 was at 150/150, normally conducive to poorer Nb(110) growth. Yet the image shows a Nb(100) film (as evidenced by the pink color in the surface image at top). Despite the presence of an amorphous, serrated pentoxide layer on the 120 nm thick seed, the subsequent film appears to follow the crystal orientation of the seed, despite annealing and coating conditions that would suggest otherwise. This supports our idea of growing a thin, high quality Nb(100) seed layer on existing bulk Nb cavities and then spraying pure molten Nb on

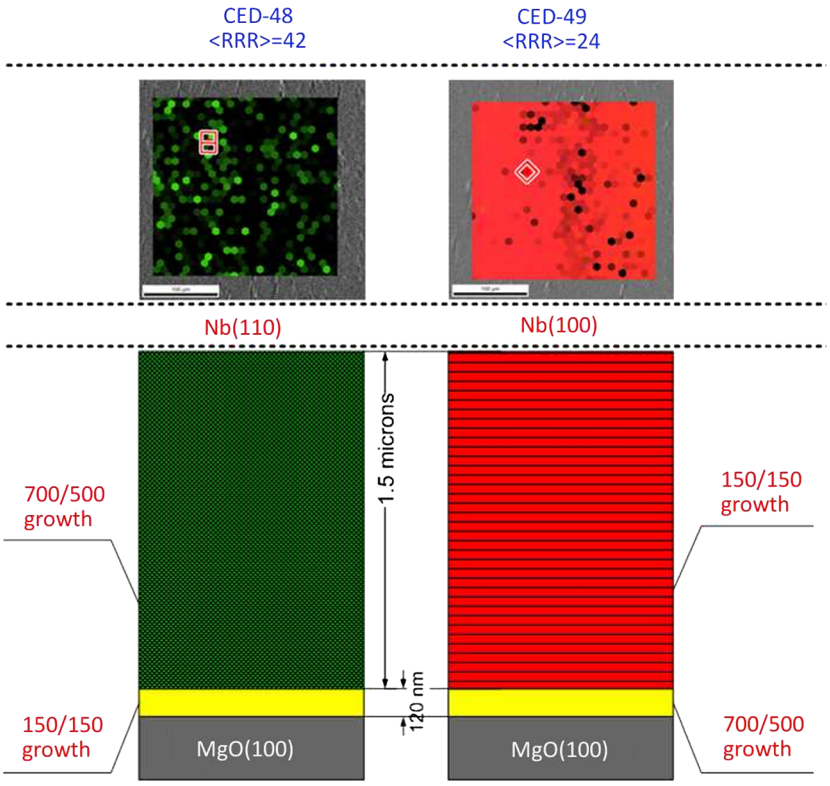

FIG. 19. Cross-section EBSD images of Nb film: CED-48 (150/150 for 120 nm followed by 700/500 for the next 1.5 μm); CED-49 (700/500 for 120 nm followed by 150/150 for the next 1.5 μm); both films were grown on MgO(100) substrate.

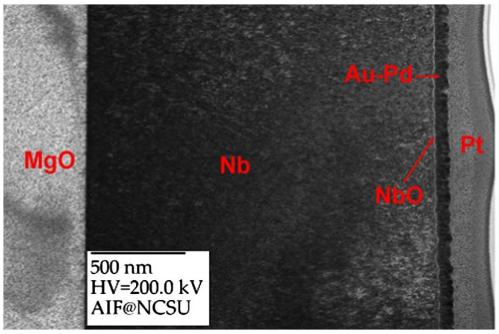

FIG. 20. TEM image of ⟨RRR⟩ = 316 Nb film on MgO.

to this seed to grow a high quality, single-crystal Nb(100) cladding layer. As observed by Kneisel [21,22], this might allow existing SRF cavities to avoid Q-slope at higher fields and boost performance of existing SRF accelerators. It is also of interest to note that for a 1–3 nm pentoxide layer, the Nb crystal growth is driven by the underlying metal lattice and not by the serrated, amorphous pentoxide.

The ⟨RRR⟩ = 24 of the Nb(100) film is lower than that (⟨RRR⟩ = 42) of the Nb(110) film. This is most likely due to the fact that the bulk of the Nb(100) film was grown at 150/150. At this lower temperature, impurities are more easily incorporated into the film and reduce its RRR. The synergistic effects of energetic condensation and thermal annealing are necessary to grow highly crystalline films with minimal defects and impurities for the best SRF properties.

X. TEM AND AFM IMAGES

Figure 20, a TEM image of a ⟨RRR⟩ = 316 Nb film on MgO shows a very smooth interface between the MgO and Nb (note the 500 nm scale bar). The film appears dense and well adhered to the surface.

Figure 21 shows AFM images of three Nb films (⟨RRR⟩ = 7, 196 and 316) all grown on MgO. The surface roughness appears to be increasing with RRR. This might be due to increasing grain size with RRR, resulting in intergrain roughness.

XI. MACROPARTICLE CRYSTAL STRUCTURE IS DRIVEN BY SEED LAYER DEPOSITED BY ENERGETIC ION CONDENSATION

Figure 22 shows a laser confocal scanning microscope image taken of a portion of the surface of the ⟨RRR⟩ = 316 Nb film grown on MgO. The figure shows what appear to be lumps on the Nb surface. These are macroparticles that are emitted by the vacuum arc, move more slowly than the ions and impinge upon the substrate.

The two macroparticles imaged vary in height from 2.1–4.5 μm and are about 10 μm in diameter. These macroparticles are molten droplets of Nb emitted at the arc cathode surface that fly from the cathode to the substrate and land there. Since these particles do not penetrate the surface (as do the ~100 eV ions), it is interesting to ask what the crystal growth modes might be in such particles, as opposed to that of the fast ions.

Figure 23 shows two cross-section SEM images taken after focused ion beam (FIB) milling of the ⟨RRR⟩ = 7 and ⟨RRR⟩ = 316 films. For the lower ⟨RRR⟩ = 7 film, the cross-section SEM shows fibrous, columnar texture in the 2.6 μm thick film. What is remarkable is that this fibrous texture continues into the ≈ 3 μm thick macroparticle that has landed on the film's surface.

With reference to Anders' SZD (see Fig. 1), the macroparticle occupies a region near the top left of the SZD, with the homologous temperature ratio, $T/T_m \sim 1$ and very low kinetic energy. In fact, since the local pressure at the cathode spots in vacuum arcs is very high (~1000 Bar), the melting point will be increased and, hence, the molten macroparticles might leave the cathode at $T/T_m > 1$. Simple estimates show that radiation from the macroparticle surface is negligible compared to the stored enthalpy, so the macro arrives at the substrate at its emitted temperature. According to the SZD, such a particle will recrystallize at the surface and acquire grain structure from the underlying substrate. Since the underlying substrate has fibrous, columnar grains (at ⟨RRR⟩ = 7) so does the condensing macroparticle. The columnar grains increase in size with height in the film, which is consistent with increase of RRR with thickness.

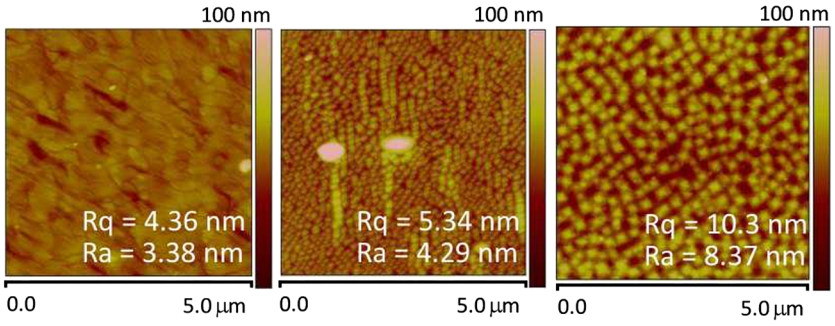

FIG. 21. AFM images of ⟨RRR⟩ = 7, 196 and 316 Nb films on MgO.

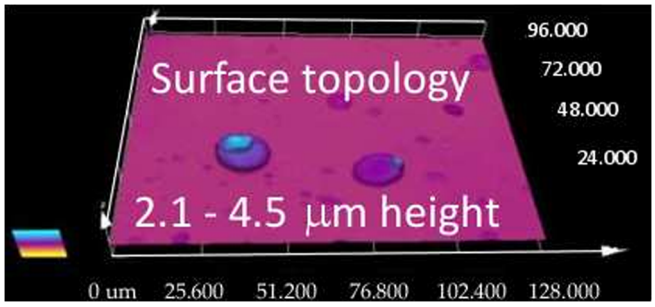

FIG. 22. Laser confocal scanning microscope (Olympus LEXT) image of ⟨RRR⟩ = 316 film.

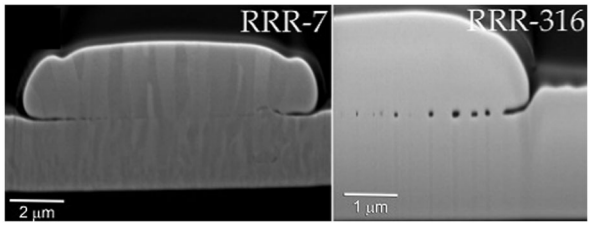

FIG. 23. FIB/cross-section SEM images of Nb films on MgO.

However, at ⟨RRR⟩ = 316, the macroparticle appears to acquire the single crystal, large grain, homoepitaxial structure of the (100) Nb film that is beneath it. This observation suggests that, once the seed layer of Nb has been grown using energetic condensation, subsequent growth maintains the properties of the seed, when slow moving, massive particles land on such a seed layer. In principle, one might first create the high quality, single crystal seed of Nb on a cavity surface, then spray high purity molten Nb on to this surface, to grow very large, single crystal Nb films.

XII. DISCUSSION

This paper has presented examples of Nb thin films grown on various crystal substrates using energetic condensation. The term energetic condensation applies to subplantation, i.e., deposition of incident ion energy within the first few subsurface atomic layers in a surface. The deposition used a cathodic arc discharge that produces a plasma of pure Nb with a kinetic energy spread of 60–120 eV, plus 46 eV of ionization potential energy, resulting in ≈ 100–170 eV energy deposition into the substrate. Each pulse deposits roughly one atomic layer of Nb in 1 ms on the substrate. This high instantaneous deposition rate minimizes impurity contamination of the film. The energetic condensation creates dense films that adhere well to the substrate. When energetic condensation is accompanied by substrate heating, the synergistic effects of the fast ion deposition and the slower thermal annealing results in a very low-defect, epitaxial film growth. The ⟨RRR⟩ was measured on *a*- and *c*-sapphire substrates as well as on MgO. Record values of ⟨RRR⟩ = 330 on *a*-sapphire and ⟨RRR⟩ = 587 on MgO are reported. ⟨RRR⟩ is found to depend strongly upon substrate temperature. The ⟨RRR⟩ is found to also depend upon film thickness. A simple model [19] shows that the RRR at the surface of the thick films might be still higher, RRR = 680 for 3 μm Nb films on MgO. XRD pole figures reveal that the crystal structure also depends strongly on substrate temperature, becoming more ordered and single-crystal as temperature is increased. On MgO, a transition from a mix of 110 and 100 planes at 500°C to purely 100 orientation at 700°C is correlated with higher RRR. The Nb(100) crystal is denser and harder than the Nb(110) crystal, as evidenced by secondary-ion mass spectroscopy depth profiling [30]. Both surface EBSD and cross-section EBSD (OIM) images corroborate the picture suggested by the bulk XRD data, of better crystal structure leading to higher RRR at higher temperatures and for thicker films. Cross-section SEM images of the films (sliced using a FIB apparatus) revealed that, when molten macroparticles of Nb land on the film grown using ion-assisted energetic condensation, the crystal structure in the condensing macroparticle is identical to that of the Nb substrate below it. This suggests another approach to cavity coating in which a high quality seed layer of Nb is first grown using our energetic condensation apparatus, that is followed by simpler condensation of molten Nb metal spray on the seed layer, thereby growing very large cladding layers inside cavities. This would be an alternative to the pioneering work done at DESY on Nb clad Cu and Cu0.15%Zr cavities [31,32].

ACKNOWLEDGMENTS

This research is supported at AASC by DOE via Grant No. DE-FG02-08ER85162 and Grant No. DE-SC0004994. The JLab effort was provided by Jefferson Science Associates, LLC under U.S. DOE Contract No. DE-AC05-06OR23177, including supplemental funding provided by the American Recovery and Reinvestment Act.

[1] H. Padamsee, J. Knobloch, and T. Hays, *RF Superconductivity for Accelerators* (John Wiley & Sons, Inc., New York, 1998).
[2] I. G. Brown, Rev. Sci. Instrum. **65**, 3061 (1994).
[3] P. Kneisel, in *SRF07* (Peking University, Beijing, China, 2007), TH102 [http://accelconf.web.cern.ch/AccelConf/srf2007/PAPERS/TH102.pdf].
[4] P. Kneisel, G. Ciovati, W. Singer, X. Singer, D. Reschke, and A. Brinkmann, in *Proceedings of the 11th European Particle Accelerator Conference, Genoa, 2008* (EPS-AG, Genoa, Italy, 2008), MOPP136.
[5] E. Valderrama, C. James, M. Krishnan, X. Zhao, L. Phillips, C. Reece, and K. Seo, in the Cryogenic Engineering Conference & International Cryogenic Materials Conference, Washington, CECICMC-11, 2011.

[6] A-M Valente-Feliciano *et al.*, in *Proceedings of the IPAC'10 Conference, Kyoto, Japan* (ICR, Kyoto, 2010).
[7] M. Krishnan, M. Geva, and J. L. Hirshfield, Phys. Rev. Lett. **46**, 36 (1981).
[8] A. Bendavid, P. J. Martin, R. P. Netterfield, G. J. Sloggett, T. J. Kinder, and C. Andrikidis, J. Mater. Sci. Lett. **12**, 322 (1993).
[9] Y. Lifshitz, S. R. Kasi, J. W. Rabalais, and W. Eckstein, Phys. Rev. B **41**, 10468 (1990).
[10] D. K. Brice, J. Y. Tsao, and S. T. Picraux, Nucl. Instrum. Methods Phys. Res., Sect. B **44**, 68 (1989).
[11] C. Thompson, J. Mech. Phys. Solids **44**, 657 (1996).
[12] A. Anders, Thin Solid Films **518**, 4087 (2010).
[13] E. Hand, Nature (London) **451**, 4 (2008).
[14] H. Padamsee, J. Knobloch, and T. Hays, 2007 RF Superconductivity for Accelerators, 2nd edition (Wiley-VCH, New York, 2008).
[15] C. Benvenuti, P. Bernard, D. Bloess, G. Cavallari, E. Chiaveri, N. Haebel, J. Hilleret, J. Tuckmantel, and W. Weingarten, in *Superconducting Niobium Sputter-Coated Copper Cavity Modules for the LEP Energy Upgrade, New York, 1991* (IEEE, New York, 1991), pp. 1023–1025.
[16] C. Benvenuti, N. Circelli, and M. Hauer, Appl. Phys. Lett. **45**, 583 (1984).
[17] S. Calatroni, Physica C **441**, 95 (2006).
[18] R. Russo, Meas. Sci. Technol. **18**, 2299 (2007).
[19] M. Krishnan, E. Valderrama, B. Bures, K. Wilson-Elliott, X. Zhao, L. Phillips, Anne-Marie Valente-Feliciano, Joshua Spradlin, C. Reece, and K. Seo, Supercond. Sci. Technol. **24**, 115002 (2011).
[20] E. Valderrama, C. James, M. Krishnan, X. Zhao, K. Seo, F. A. Stevie, and P. Maheshwari, in Proceedings of 15th International Conference on RF Superconductivity, Chicago, 2009, THPO077.
[21] A. Anders, Phys. Rev. E **55**, 969 (1997).
[22] A. Andreone, A. Cassinese, M. Iavarone, R. Vaglio, I. I. Kulik, and V. Palmieri, Phys. Rev. B **52**, 4473 (1995).
[23] C. Attanasio, L. Maritato, and R. Vaglio, Phys. Rev. B **43**, 6128 (1991).
[24] T. L. Hylton, A. Kapitulnik, M. R. Beasley, J. P. Carini, L. Drabek, and G. Gruner, IEEE Trans. Magn. **25**, 810 (1989).
[25] O. G. Vendik, A. B. Kozyrev, and A. Yu. Popov, Zh. Tekh. Fiz. **59**, 107 (1989) [Sov. Phys. Tech. Phys. **34**, 62 (1989)].
[26] B. D. Cullity and S. R. Stock, *Elements of X-ray diffraction* (Prentice-Hall, Englewood Cliffs, NJ, 2001), Chap. 14.
[27] X. Zhao, L. Philips, C. E. Reece, K. Seo, M. Krishnan, and E. Valderrama, J. Appl. Phys. **110**, 033523 (2011).
[28] D. Baars *et al.*, *SRF Workshop 2007* (Peking University, Beijing, 2007), TH102 [http://accelconf.web.cern.ch/AccelConf/srf2007/PAPERS/TUP05.pdf].
[29] J. Halbritter, J. Less-Common Met. **139**, 133 (1988); Appl. Phys. A **43**, 1 (1987).
[30] M. Krishnan, E. Valderrama, C. James, X. Zhao, J. Spradlin, A-M Valente Feliciano, L. Phillips, C. Reece, Z. H. Sung, F. A. Stevie, P. Maheshwari, and D. Batchelor, in Proceedings of the 15th International Conference on RF Superconductivity, Chicago, IL (2011), TUIOB01.
[31] W. Singer, in the 13th International Workshop on RF Superconductivity, 2007, Beijing, China.
[32] X. Singer, W. Singer, I. Jelezov, A. Matheisen, and P. Kneisel, in *Proceedings of the 23rd Particle Accelerator Conference, Vancouver, Canada, 2009* (IEEE, Piscataway, NJ, 2009) [http://trshare.triumf.ca/Epac09proc/Proceedings/papers/tu5pfp055.pdf].